Constraints on the Near-Field Surface Displacement Gradient of the Landers Earthquake Imposed by Radar Interferometry

Gilles Peltzer
Jet Propulsion Laboratory, California Institute of Technology, Pasadena, California

Kenneth W. Hudnut,
US Geological Survey, Pasadena, California

Kurt L. Feigl
CNRS UPR 234, Observatoire Midi-Pyreenes, Toulouse, France

Submitted to JGR, February 17, 1994

Please address correspondence to:
Gilles Peltzer
JPL/MS 183-501
4800 Oak Grove Drive
Pasadena, CA 91109
Tel. (818) 354-75 39, Fax (818)354-50 59
Email, gilles@altyn.jpl.nasa.gov

Abstract

The map of the co-seismic displacement field generated by interferometric processing of Synthetic Aperture Radar (SAR) images taken before and after the June 28, 1992 Landers earthquake sequence brings new insights into the nature of deformation caused by these earthquakes. In the intermediate and far fields, the displacement map is consistent with the predictions of a simple elastic dislocation model. In the vicinity of the surface rupture, however, the pattern of interferometric fringes appears to be more dense and complex than in the model. This complexity reflects short wavelength variations of the surface rupture and slip distribution, and attests to large displacement gradients. In some sections of the fault with overlapping branches, the interferogram loses coherence and no fringes can be recognized. In these areas, the ground displacement gradient was probably large enough to create more than one fringe per 90m-pixel of the radar image and cause the de-correlation. In other sections of the fault, very dense fringe patterns can be recognized, contrasting in density and direction with patterns observed away from the rupture. In order to understand the observed fringe patterns, we compute synthetic interferograms in three simple cases: (1) rigid-body rotations about a vertical axis, (2) about a horizontal axis (tilt), and (3) distributed, simple shear.

Where the Kickapoo fault connects with the Homestead Valley fault, the interferogram shows a clear pattern of parallel N20°W fringes separated by about 160 m. This pattern and vertical offsets measured along the Kickapoo fault suggest that the block between this fault and the Johnson Valley fault may have been tilted westward. Simple simulations show that a 5-km block lifted by 1 m on one side would be tilted by an angle of 0.01°

surface displacement vector requires independent observations and some modeling.

For the Landers earthquake, a simple elastic dislocation model, based on the rupture map and surface offset measurements at the fault, appears to account for most of the fringes observed in the far and intermediate fields [Massonnet et al., 1993]. In most places, the difference between the observed and predicted range displacement is less than 2 cycles (56.6 mm). Within 5 km from the faults, however, the rupture pattern involved important secondary faulting, overlapping segments and numerous fissures, resulting in a complex displacement field depicted by dense fringe patterns and zones of incoherence in the interferogram (Figure 1) which are not accounted for by the simple elastic model described in Massonnet et al. [1993]. In an attempt to understand the small scale features of the Landers earthquake interferogram in the vicinity of the fault breaks, we compute synthetic interferograms for simple examples of displacement field that one may expect near a fault surface rupture. We then compare these synthetic interferograms with the fringe patterns observed at two selected areas along the fault. These areas include (1) the northern end of the Johnson Valley fault, where it merges with the Kickapoo (or Landers) fault, and (2) the surface rupture gap between the southern end of the Johnson Valley fault and the Eureka Peak fault. For these two sites, we confront the inferences based on the radar interferogram with field observations and results of inversion of geodetic data.

Examples of simple fringe pattern

In order to understand the complexity of the patterns observed in the interferogram in the vicinity of the rupture, we compute synthetic interferograms produced in three simple cases: (1) rigid-body rotation about a vertical axis, (2) about a horizontal axis (tilt), and (3) distributed simple shear. For each of these three cases, we compute the slant range component of the ground point displacement vectors and derive the orientation of the fringes and their spatial separation. The slant range component of a horizontal displacement vector is the projection of that vector onto the satellite cross-track direction multiplied by the sine of the look angle. Similarly, the range component of a vertical displacement vector is the magnitude of that vector multiplied by the cosine of the look angle.

The domains in which such simple deformation figures occur are unlikely to extend more than 2 to 5 kilometers across the SAR image swath, i.e., approximately the distance between overlapping branches of the fault. Hence we assume that the satellite look angle (the angle between the satellite line of sight and the vertical) remains constant across the area involved. Since the near and far range look angles for ERS-1 SAR images are 19° and 27°, respectively, we use the average value of 23°.

Rigid-body rotation

Figure 2a shows the case of a rigid-body rotation of a crustal block about a vertical axis. The projection of the incremental displacement vector onto the cross-track direction remains constant along straight lines parallel to that direction. Therefore fringes, which are lines of equal displacement in the range direction, are straight lines trending perpendicular to the

satellite track direction. For a small rotation angle r, the distance between consecutive fringes is given by

$$d_r=\lambda/[2\ r\ \sin(\beta)], \qquad (1)$$

where λ is the radar wavelength (56.6 mm) and β, the look angle (23°). Figure 2b shows the case of a tilted crustal block, i.e., a rigid-body rotation about a horizontal axis. For a small rotation angle t, the displacement vectors of ground points are essentially vertical and remain constant along straight lines parallel to the tilt axis. The fringes are thus parallel to the tilt axis and the interval between consecutive fringes is given by

$$d_t=\lambda/[2\ t\ \cos(\beta)]. \qquad (2)$$

Synthetic interferograms corresponding to the two rotation cases above and for various angles of rotation are shown in Figure 3a. Figure 3b depicts the variation of distances d_r and d_t with rotation angles r and t, respectively. For a rotation angle of about 0.2° and a tilt angle of about 0.1°, the distance between fringes is of the same order of magnitude as the size of the SAR full-resolution image pixel (20m in range for the ERS-1 SAR). This means that for angles greater than these values the interferogram becomes incoherent because the phase variation across each pixel exceeds one cycle. Zebker and Villasenor [1992] have studied the decorrelation of interferometric radar echoes resulting from change in the apparent distributions of scatterers within each image pixel. Their results show in particular that the signal decorrelates completely for rotation angles of about 0.7° at C-band. The limiting value of 0.2° noted above for horizontal rotations, which depends on the size of the ERS-1 SAR image pixel, is reached before signal decorrelation occurs in the sense of Zebker and Villasenor [1992]. For the interferogram of the Landers earthquake, the radar data have been averaged over 90 m pixels in order to match the

resolution of the USGS digital elevation model used to remove the topographic signal [Massonnet et al., 1993] (Figure 1). For such a pixel size, the limiting rotation angle value is even smaller. Fringes produced by block rotations or tilts become invisible for rotation angles exceeding values of approximately 0.02° and 0.01°, respectively (Nyquist effect, Figure 3b). The technique of averaging the radar signal over several pixels (multi-looking) is commonly used for noise reduction. Because it degrades the resolution of the image, it is inappropriate for imaging areas of high displacement gradient [Goldstein et al., 1993].

Distributed shear

In a shear zone where simple shear is evenly distributed across a zone of finite width, the displacement of a ground point in the shear zone is proportional to the distance between the point and the edge of the shear zone (Figure 2c). The displacement vectors remain constant along straight lines parallel to the shear direction and the resulting fringes are thus parallel to that direction. The distance between consecutive fringes is given by

$$d_S=\lambda/(2\,\gamma\,\sin(\delta-\alpha)\,\sin(\beta)), \qquad (3)$$

where α is the satellite track azimuth, δ, the shear zone azimuth and γ, the shear coefficient. Note that for shear zones striking in the direction of the satellite track ($\delta=\alpha$), this distance is not defined. This is due to the fact that any displacement of the ground in the direction of the satellite track has a null projection onto the range axis. Therefore, a distributed shear zone parallel to the satellite track would not produce any fringes in an interferogram.

Any combination of the simple cases considered above would result in complex fringe patterns which may be difficult to predict and interpret uniquely. However, by combining the information provided by the interferogram with independent field observations of the geometry of the rupture and offset distribution, simple models can be constrained. In the following sections, we analyze the co-seismic displacement field in the vicinity of the Landers earthquake rupture zone and examine in detail two segments of the fault where dense fringe patterns are observed.

Quantitative Analysis of the Displacement Gradient in the Vicinity of the Rupture

One of the most striking features apparent in the Landers earthquake co-seismic interferogram near the fault is the narrow band with no coherent fringes along most of the fault (Figure 1). Although many changes due to the violent ground motion may have affected the ground surface during the earthquake, the most likely reason for such a decorrelation is the increase of the displacement gradient in the vicinity of the rupture [Zebker and Villasenor, 1992; Massonnet et al., 1993; Zebker et al., 1994b]. High displacement gradients produce dense interferometric fringe patterns which cannot be depicted in a digital image when the distance between the fringes becomes smaller than the size of the image pixel. In our study, the limiting threshold is the 90-meter pixel size of the radar image once averaged in order to match the resolution of the USGS digital elevation model used in the data processing [Massonnet et al., 1993]. Using the full-resolution SAR images would help in analyzing regions of high strain provided that the data noise is sufficiently low [e.g., Goldstein

et al., 1993]. In some areas along the fault where detailed mapping has been done, numerous secondary faulting and fissures are reported, attesting to high strain within the rocks adjacent to the main surface break [e.g., Sieh, et al., 1993; Johnson et al., 1993; Hart et al., 1993; Sowers et al., 1994]. Studying the deformation field in such areas is beyond the present capability of the interferometric technique given the resolution of the ERS-1 SAR data.

The Johnson Valley fault -Kickapoo fault junction

The Kickapoo fault (a.k.a. the Landers fault [Sieh et al., 1993]) crosses from the northern Johnson Valley fault towards the southern Homestead Valley fault, where these two faults overlap over a distance of 6 km (Figure 4). The distribution of co-seismic lateral displacement along these three faults shows that the Kickapoo fault progressively transfers the 3-4 meters of right lateral slip from the Johnson Valley fault to the Homestead Valley fault (Sowers et al., 1994). We focused on the wedge-shaped area between the Johnson Valley and the Kickapoo faults primarily because the interferogram there shows a dense pattern of parallel fringes which contrasts markedly in density and orientation with the fringe patterns observed both west of the Johnson Valley fault and east of the Homestead Valley fault (Figure 4). Between the faults, the fringes are closely spaced and trend about N160°E, parallel to the local strike of the Johnson Valley and Homestead Valley faults, whereas, on the opposite sides of these two faults, the fringes are widely spaced and merge with the fault trace at a high angle. Our first interpretation of this pattern was that the wedge-shaped block bounded by the Johnson valley and the Kickapoo faults might have rotated clockwise as one would expect to see between right-

stepping, overlapping, right-lateral fault segments [e.g., Scotti et al., 1990]. However, Figure 2a and the simulation of rotating blocks about a vertical axis (Figure 3a) show that such rotations would produce fringes perpendicular to the satellite track (i.e., an azimuth of 100°E). The fact that the observed fringes strike parallel to the local direction of the Johnson Valley and Homestead Valley faults suggests instead that the strike of these faults control the deformation or displacement of this block by imposing either the direction of shear, in the case of simple, distributed shear, or the azimuth of the rotation axis in the case of a tilted block. We have shown in the previous section that in both of these cases the fringes would be parallel to the Johnson Valley and Homestead Valley faults. Deciding between these two hypotheses cannot be done using solely the information provided by the interferogram which depicts only one component of the surface displacement field. However, the consistently equidistant, parallel fringes across an area of ~2x5 km implies a departure from an elastic behavior. In an elastic shear zone, the displacement gradient, and thus the density of the fringes, are expected to decrease gradually from the center to the edge of the shear zone. In the case of block tilting, the equidistant fringes imply a nearly rigid behavior. The fact that significant vertical offsets occurred along the various fault segments involved seems to support the tilted block hypothesis as opposed to distributed shear which would not involve much vertical displacement.

Vertical offsets along the Johnson Valley fault produced east-facing scarps north of the junction with the Kickapoo fault, and west facing scarps south of it, suggesting differential vertical displacements of the block north of the junction with respect to the block south of it. Vertical offsets along the Kickapoo fault and localized reverse displacement on the "slip gap"

segment of the Homestead Valley fault both indicate relative uplift of the western compartment. A down-to-the-southwest tilt of the block bounded by the Johnson Valley and the Kickapoo faults about an axis trending N160°E would explain both the vertical offsets observed in the field and the dense fringe pattern observed in the interferogram.

Assuming that the block between the Johnson Valley and the Kickapoo faults has been tilted during the earthquake, it is possible to quantify the direction and amount of tilt from the interferogram. First, the tilt axis must be parallel to the local direction of fringes, i.e. ~N160°E. Second, the variation of the phase within a cycle indicates that the displacement of the ground towards the satellite (uplift) increases with the distance northeast from the Johnson Valley fault. This suggests that the tilt is down towards the southwest. Third, the average distance between consecutive fringes along a 1.5-km-long profile in the zone of dense fringe pattern is d_t=162±10 m. This value and equation (2) allow us to constrain the tilt angle to be t=0.01°±0.005° (190±10 μrad), assuming the satellite look angle to be constant at 23°. The error in these values reflects only the variations in length of profiles along which ten fringes could be counted in the interferogram. The direction and amount of tilt inferred from the interferogram appear to be generally consistent with the distribution of vertical offset observed along the Kickapoo fault. Figure 5 shows that the vertical offsets measured along the Kickapoo fault and along the thrust segment of the Homestead Valley fault [Sieh et al., 1993; Hart et al., 1993] increase northeastward with the distance from the Johnson Valley fault. Although measurements along the Kickapoo fault show local variations due to its complex, en échelon geometry, this distribution can be mostly accounted for by a westward tilt of 0.01° of the westward compartment.

Analysis of the morphology of the Homestead valley [Sowers et al., 1994] and paleoseismic studies [Rockwell et al., 1993] show that these faults have been active during the Quaternary and may have previously ruptured in the manner of the 1992 earthquake. If the block between the Johnson Valley and the Kickapoo faults has been repeatedly tilted with past earthquakes, the cumulative effect of such tilts should be recorded in the topography. Figure 6a shows a topographic profile leveled perpendicular to the Johnson Valley fault and Figure 6b the elevation profile from which the average slope profile was subtracted. Although slopes of alluvial fans are generally concave up [e.g., Troeh, 1965], a break in the slope of profile in Figure 6b is clear and is consistent with a westward tilt of the northeast compartment. Exponential curves adjusted with the upper (AB) and lower (CD) parts of the profile, respectively, intersect at an angle of 0.15°, about fifteen times the co-seismic tilt angle inferred above for the 1992 event. Geologic mapping and gravity measurements of the area indicate the existence of an east facing subsurface bedrock escarpment associated with the northern Johnson Valley fault [Sowers et al., 1994]. By contrast, the data do not indicate long term, cumulative vertical displacement across the Kickapoo fault. These observations suggest that, if similar block tilting repeatedly occurred with earthquakes, it was associated with the subsidence of the western part of the block, against the Johnson Valley fault plane rather than with the uplift of its eastern side, as the 1992 east-facing scarps observed along the Kickapoo fault suggest. Finally, the tilted block model involving some thrust component of displacement along the adjacent segment of the Homestead Valley fault is consistent with the through-going model, as opposed to the step over model, both discussed in Sowers et al. [1994].

The Johnson Valley-Eureka peak surface rupture gap

The surface fault breaks along the Johnson Valley fault die out north of Yucca Valley and reappear south of the Pinto Mountain Fault, along the Burnt Mountain and Eureka Peak faults [Sieh et al., 1993, Hart et al., 1993]. In this 6.5 km-long gap in surface breaks, the interferogram shows a pattern of dense fringes roughly parallel to the local direction of the southern Johnson Valley and Eureka Peak faults, suggesting that slip took place at depth on this segment (Figure 7). This is also suggested by the continuous distribution of aftershocks along this segment [Hauksson et al., 1993]. A more convincing evidence of a continuous north-trending fault break comes from the seismic guided waves generated by aftershocks and trapped in the low velocity fault zone [Li et al., 1994]. These trapped Love waves reveal a ~180-m-wide low velocity zone extending continuously through the intersection with the Pinto Mountain fault [Li et al., 1994]. The surface expression of strike-slip displacement occurring on a buried fault would be a zone of distributed shear parallel to the fault direction. We have shown in the previous section that distributed shear results in dense fringes parallel to the shear direction (Figure 2c), similar to the pattern observed between the Johnson Valley fault and the Eureka Peak fault ruptures (Figure 7). The average distance between consecutive fringes measured along a 3.6 km long profile, perpendicular to the shear direction is d_S=331 m. With a shear direction of δ=130°, the satellite track azimuth α=10°, the radar wave length λ=56.6 mm and the look angle β=23°, equation (3) allows us to compute the shear coefficient $\gamma=2.9\times10^{-4}$ of the shear zone. Such a shear may be produced by a right-lateral displacement of 1 meter, distributed over a 3.6 km wide shear zone. Although we don't have any

independent observation to directly test this inference, it is interesting to note that results of inversion of geodetic data imply 0.8 to 1.8 of right-lateral slip at depth in the gap [e.g., Hudnut and Larsen, 1994; Wald and Heaton, 1994] (Figure 8). However, such inversions do not have the resolution for solving details such as the depth of the locked zone above the rupture plane in the surface break gap. The SAR interferogram helps constrain this depth. If the width of the intense shear zone is about twice the depth of the fault, then the top of the rupture plane must be about 1.5-2 km below the surface between the Johnson Valley and the Eureka Peak faults. Figure 9 shows synthetic interferograms obtained by elastic dislocation modeling for three different fault depths in the surface rupture gap. The elastic model covers a 15 km by 15 km area centered on the surface breaks gap. The southern Johnson Valley fault, the Eureka Peak fault and the blind fault in the gap are modeled as three vertical planes. The distribution of slip at depth for these three faults is based on results of inversion of geodetic data [Hudnut and Larsen, 1994]. The fault segment in the gap is locked above depths of 0.5, 1.5, and 2.5 kilometers in the three modeled cases. Comparison of fringe spacing in the shear zone between the co-seismic interferogram (Figure 7) and the modeled interferograms (Figure 9) shows that a locking depth of approximately 1.5 km in the rupture gap would account for the observed fringe pattern.

Discussion and Conclusion

The SAR interferogram has brought new insights into displacement gradients in the vicinity of the Landers fault rupture. Because of the high sensitivity of the technique to the ground displacements, extremely small

gradients of the displacement field can be measured. Between the northern end of the Johnson Valley fault and the Kickapoo fault, the interferogram shows a dense pattern of parallel fringes consistent with a rigid block tilt (down to the southwest) of the ~3x5 km crustal block bounded by these faults of about 0.01° (190 μrad). In the surface rupture gap between the Johnson Valley and the Eureka Peak faults, the pattern of dense fringes can be accounted for by a distributed shear produced by 1 meter of slip on a "blind" segment of the fault, with slip occurring at depth greater than 1.5 km. Similar dense patterns of fringes are barely visible between the Homestead Valley and Emerson faults but the level of noise in the interferogram in this area prevented us from clearly interpreting the ground displacement gradient there. We have shown that rigid-body rotations about a vertical axis would produce characteristic fringes perpendicular to the satellite track. We did not observe such patterns in the coherent part of the interferogram near the fault.

In most other sections of the fault, the interferogram shows a zone of apparent decorrelation in the vicinity of the rupture. Two reasons can be advanced for the loss of coherence near the fault. First, some segments of the fault follow mountain ranges with rough topographic terrain reducing the level of correlation between the two SAR images [Zebker et al., 1994a]. This problem could be partly overcome by using a pair of SAR images acquired from orbits closer together, thus reducing the sensitivity of the interferogram to topography [Li and Goldstein, 1990]. Second, the displacement gradient in those areas near the fault is sufficiently large to produce more than one phase cycle per image pixel. Given the resolution of 20m in range of the ERS-1 SAR images, the threshold gradient above which the coherence is lost is around 1 per 1000. In cases where the noise

in the data requires averaging over several SAR pixels, the above value is reduced by the averaging factor. The technique is thus not best adapted to studying natural processes involving high strain of the Earth's surface. At the other end of the spectrum, extremely small displacements can be detected readily and the limit of detection varies, depending on the ability to smooth the data for phase noise reduction and on the surface area involved with a consistent strain pattern. Given the limitations we discuss, we have shown that it is possible to map the displacement field resulting from a large earthquake with a level of detail not attainable by other geodetic techniques. For smaller or deeper earthquakes, producing smaller displacement gradients at the surface, the SAR interferometry technique provides a powerful way of investigating short wavelength features of the surface displacement field bringing new insights into earthquake rupture processes and fault segmentation.

Acknowledgments: We would like to thank the many geologists of the surface faulting mapping groups at Caltech, led by K. Sieh, and at USGS-Menlo Park, led by K. LaJoie, as well as T. Rockwell, S. Lindvall and Janet Sowers for sharing their results in advance of publication. We also thank E. Ivins for his comments on the early version of the manuscript. The research described in this paper was carried out by the Jet Propulsion Laboratory under contract with the National Aeronautics and Space Administration.

References

Goldstein, R.M., H. Engelhardt, B. Kamb, and R.M. Frolich, Satellite Radar Interferometry for monitoring ice sheet motion: application to an Antarctic ice stream, Science, 262, 1525-1530, 1993.

Hauksson, E, L.M. Jones, K. Hutton, and D. Eberhart-Phillips, The 1992, Landers earthquake sequence: seismological observations, J. Geophys. Res., in press, 1993.

Hart, E.W., W.A. Bryant, and J.A. Treiman, Surface faulting associated with the June 1992 Landers earthquake, California, Calif. Geol., 46, 10-16, 1993.

Hudnut, K.W., and S.C. Larsen, Slip distribution in the 1992 Landers, California earthquake sequence determined from geodetic data, J. Geophys. Res., submitted, 1994.

Johnson A.M., R.W. Fleming, and K.M. Cruikshanl, Broad belts of shear zones as the common form of surface rupture produced by the 28 June 1992 Landers, California earthquake, U.S.G.S. open-file report, 93-348, 1993.

Li, F. and R.M. Goldstein, Studies of multi-baseline spaceborne interferometric synthetic aperture radars, IEEE Trans. Geosci. Remote Sensing, 28, 88-97, 1990.

Li, Y.-G., K. Aki, D. Adams, A. Hasemi, and W. H. K. Lee, Seismic guided waves trapped in the fault zone of the Landers, California, earthquake of 1992, in press, 1994.

Massonnet, D., M. Rossi, C. Carmona, F. Adragna, G. Peltzer, K. Feigl, and T. Rabaute, The displacement field of the Landers earthquake mapped by radar interferometry, Nature, 364, 6433, 138-142, 1993.

Nur, A., H. Ron, and O. Scotti, Fault mechanics and the Kinematics of block rotations, Geology, 14, 746-749, 1986.

Rockwell, T.K., D.P. Schwartz, K. Sieh, C. Rubin, S. Lindvall, M. Herzberg, D. Padgett, and T. Fumal, Initial paleoseismic studies following the Landers earthquake: implication for fault segmentation and earthquake clustering, EOS Trans., AGU, 74, 43, 67, 1993.

Sieh, K., L. Jones, E. Haukson, K. Hudnut, D. Eberhart-Phillips, T. Heaton, S. Hough, K. Hutton, H. Kanamori, A. Lilje, S. Lindvall, S. McGill, J. Mori, C. Rubin, J. Spotila, J. Stock, Hong Kie Thio, J. Treiman, B. Wernicke, and J. Zachariasen, Near-field investigations of the Landers earthquake sequence, April to July 1992, Science, 260, pp171-176, 1993.

Sowers, J.M., J.R. Unruh, W.R. Lettis, and T.D. Rubin, Relationship of the Kickapoo fault to the Johnson Valley and Homestead Valley faults, San Bernardino county, California, BSSA, in press, 1994.

Troeh, F.R., Landform equations fitted to contour maps, Am. J. of Sc., 263, 616-627, 1965.

Wald, D. and T. Heaton, Spatial and temporal distribution of slip for the 1992 Landers, California earthquake, Seism. Soc. of Am. Bull., in press, 1994.

Zebker, H.A., and J.Villasenor, Decorrelation in interferomtetric radar echoes, IEEE Trans. on Geosci. and Rem. Sens., 30, 5, 950-959, 1992.

Zebker, H.A., C. Werner, P. Rosen, and S. Hensley, Accuracy of topographic maps derived from ERS-1 interferometric radar, IEEE Trans. Geosc. and Rem. Sens., submitted, 1994a.

Zebker, H. A., P. Rosen, R.M. Goldstein, A. Gabriel, and C.L. Werner, On the derivation of coseismic displacement fields using differential radar interferometry: the Landers earthquake, J. Geophys. Res., submitted, 1994b.

Figure captions:

Fig. 1. Co-seismic interferogram of the Landers, June 28, 1992 earthquake obtained with ERS-1 SAR data (after Massonnet et al., 1993). Fringes are contour lines of equal displacmeent of the ground along line of sight of the satellite. One full grey-scale cycle represents 2.8 cm of surface displacement. Surface rupture, shown in white, is from Hart et al., 1993. Boxes delineate areas of Figures 4 and 7.

Fig. 2. a. Sketch in map view showing geometry of displacement vector in the case of rigid-body rotation about a vertical axis. Projection AA" of displacement vector AA' onto satellite cross-track direction AB is constant along that direction. Fringes are thus parallel to that direction, i.e., perpendicular to satellite track direction. For a small rotation angle r, fringe separation is $d_r=\lambda/(2\ r\ \sin(\beta))$, where λ is radar wavelength (56.6 mm) and β the satellite look angle.

Fig. 2. b. Sketch in perspective view showing displacement vector in case the of rigid-body rotation about a horizontal axis (tilt). For small rotation angle t, displacement vector MM' is vertical and proportional to distance MK to tilt axis. Vector MM' and its projection MM" onto satellite line of sight is constant along lines parallel to tilt axis assuming look angle β constant. Fringes are thus parallel to tilt axis and fringe separation is $d_t=\lambda/(2\ t\ \cos(\beta))$.

Fig. 2. c. Sketch in map view showing displacement vector in the case of simple, distributed shear. Displacement vector MM' is proportional to

distance KM to edge of shear zone. Projection MM" of MM' onto cross track direction is constant along lines parallel to the shear direction. Fringes are thus parallel to the shear direction. Fringe separation is $d_S=\lambda/(2\ \gamma \sin(\delta-\alpha) \sin(\beta))$, where γ is shear coefficient, δ, shear direction azimuth and α, satellite track azimuth.

Fig. 3. a. Synthetic interferograms generated in the case of rigid-body rotations about a vertical axis (upper row) and tilts (lower row) for five different rotation angles. Rotation angles are indicated in degrees. Size of boxes represents 5 km on the ground and image pixel is assumed to be 90 m, as for the Landers earthquake interferogram of Figure 1. Fringes are perpendicular to satellite track direction (N20°E in shown example) for rotations about vertical axis and parallel to rotation axis (N160°E in shown example) for tilts.

Fig. 3. b. Curves showing decrease of fringe separation with increasing rotation angle in cases of Figure 3 a.

Fig. 4. Detail of co-seismic interferogram of Figure 1 in the area of the Johnson Valley, Kickapoo, Homestead Valley faults junction. Surface rupture is from Sieh et al. [1993], and Sowers et al. [1994].

Fig. 5. Variation of vertical offset measured along the Kickapoo and the southern Homestead Valley faults (west side up) as function of distance from Johnson Valley fault. Straight line indicates vertical offset predicted by tilted block model with tilt angle of 0.01° (190 μrad).

Fig. 6.a. Topographic profile levelled prependicular to the Johnson Valley fault. Origin of x axis is at the fault and values are positive towards the northeast. Vertical exageration is 7.7 to 1. Topographic data are from USGS 7.5 minutes map.

Fig. 6. b. Same profile as in Figure 6 a with average slope 2.39° substracted. Vertical exageration is 127 to 1.

Fig. 7. Detail of the co-seismic interferogram of Figure 1 in area of surface rupture gap between Johnson Valley and Eureka Peak faults. Fault traces from Sieh et al. [1993].

Fig. 8. Distribution of slip at depth in the Johnson Valley, Eureka Peak faults surface rupture gap derived from inversion of geodetic data [Hudnut and Larsen, 1994].

Fig. 9. Synthetic interferograms obtained by elastic dislocation modeling for three different locking depths in surface rupture gap between the Johnson Valley and Eureka Peak faults. Slip distribution at depth is from results of inversion of geodetic data [Hudnut and Larsen, 1994]. Fault depth in gap is indicated. White lines are surface traces of Johnson Valley (top left) and Eureka Peak (bottom right) faults as modeled. Blind fault connecting these two faults at depth is not shown.

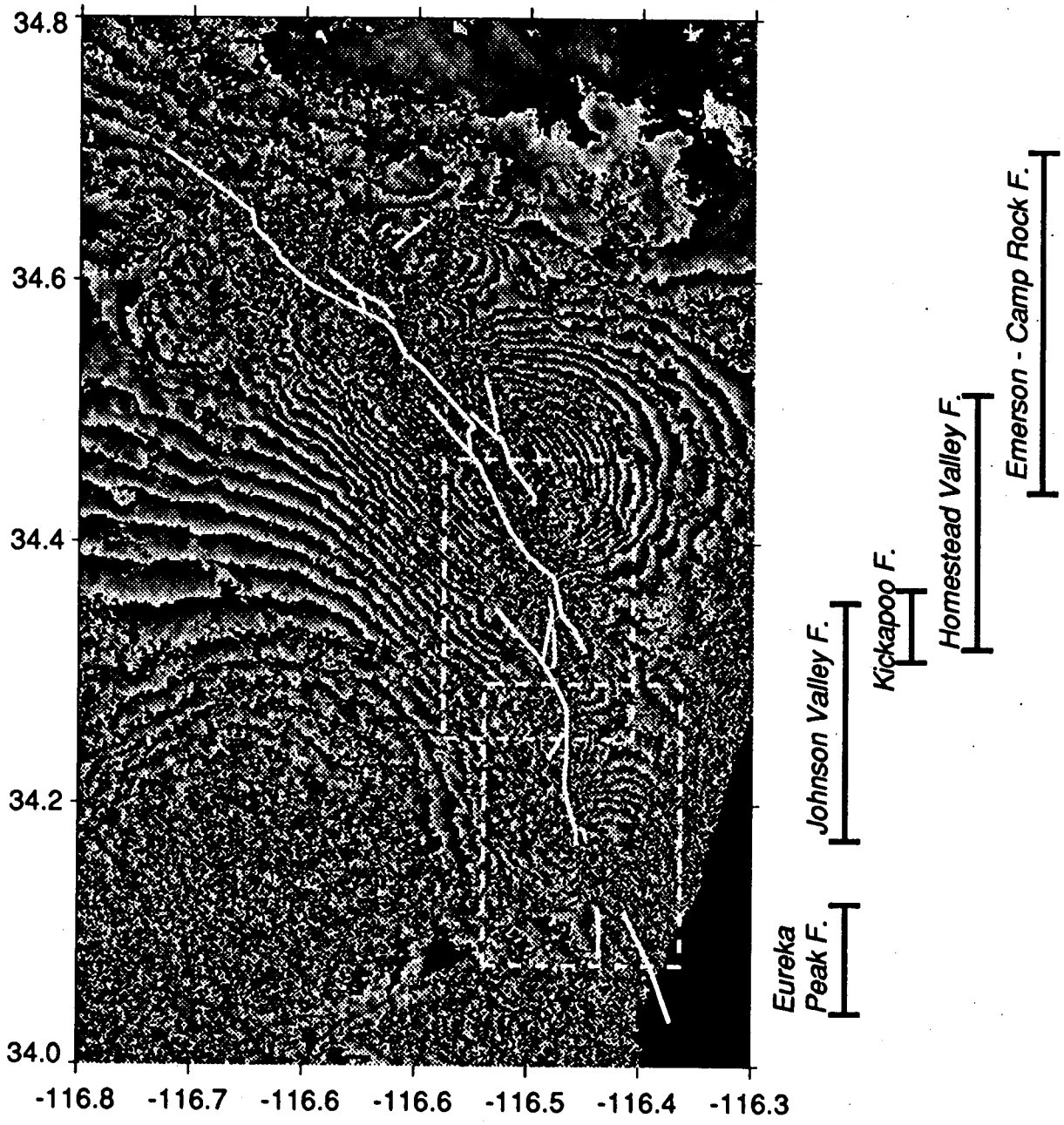
34.8
34.6
34.4
34.2
34.0
-116.8
-116.7
-116.6
-116.6
-116.5
-116.4
-116.3
Eureka Peak F.
Johnson Valley F.
Kickapoo F.
Homestead Valley F.
Emerson - Camp Rock F.

Figure 1

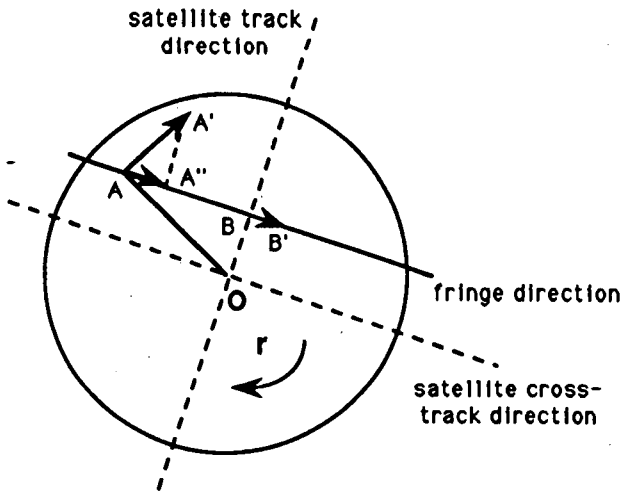
satellite track direction
A'
A''
A
B
B'
O
r
fringe direction
satellite cross-track direction

a

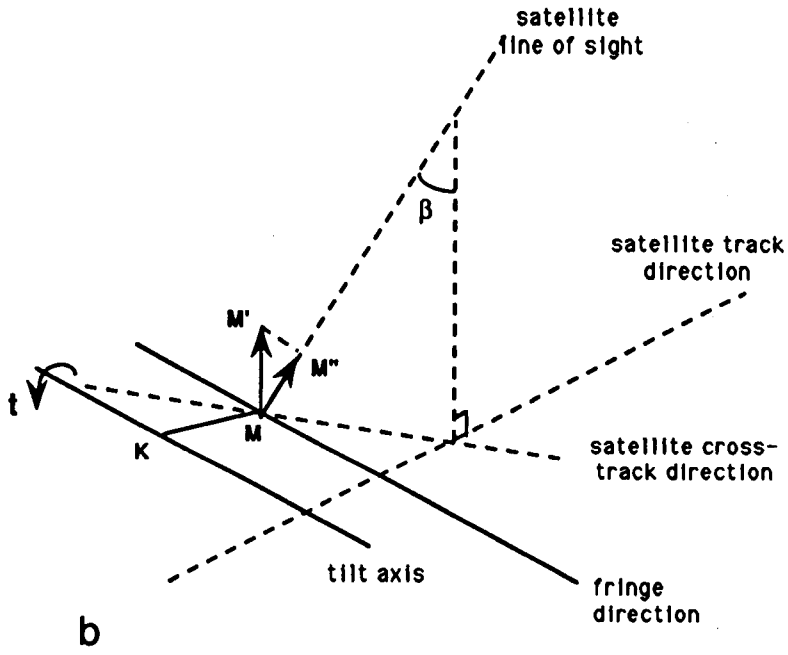
satellite line of sight
β
satellite track direction
M'
M''
t
M
K
satellite cross-track direction
tilt axis
fringe direction

b

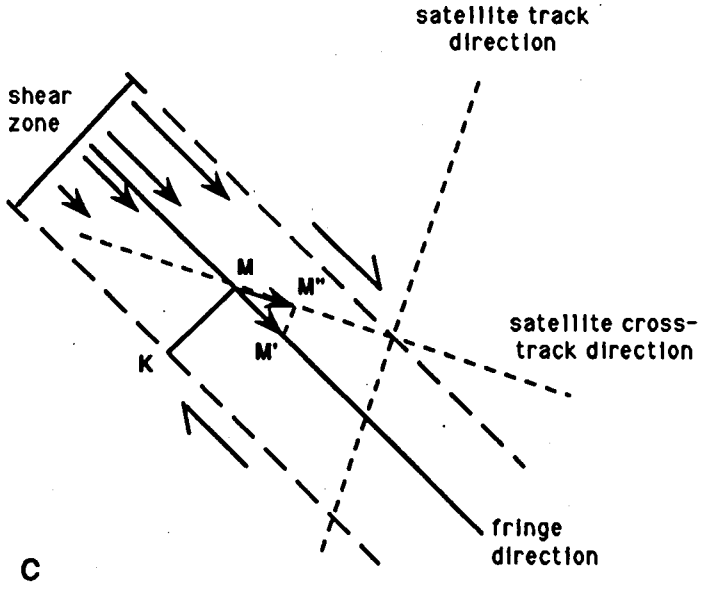
satellite track direction
shear zone
M
M''
M'
K
satellite cross-track direction
fringe direction

c

Figure 2

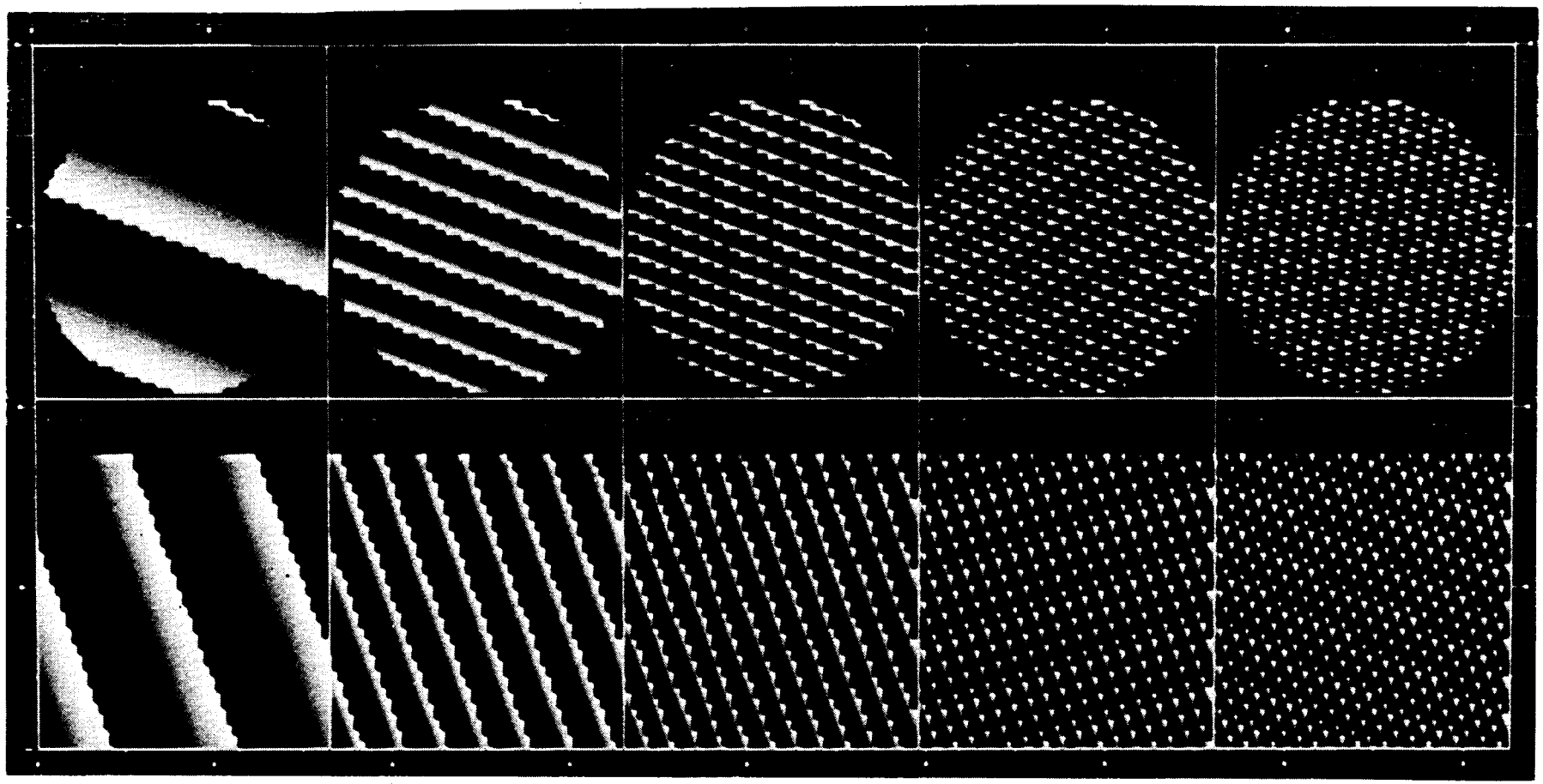

Figure 3a

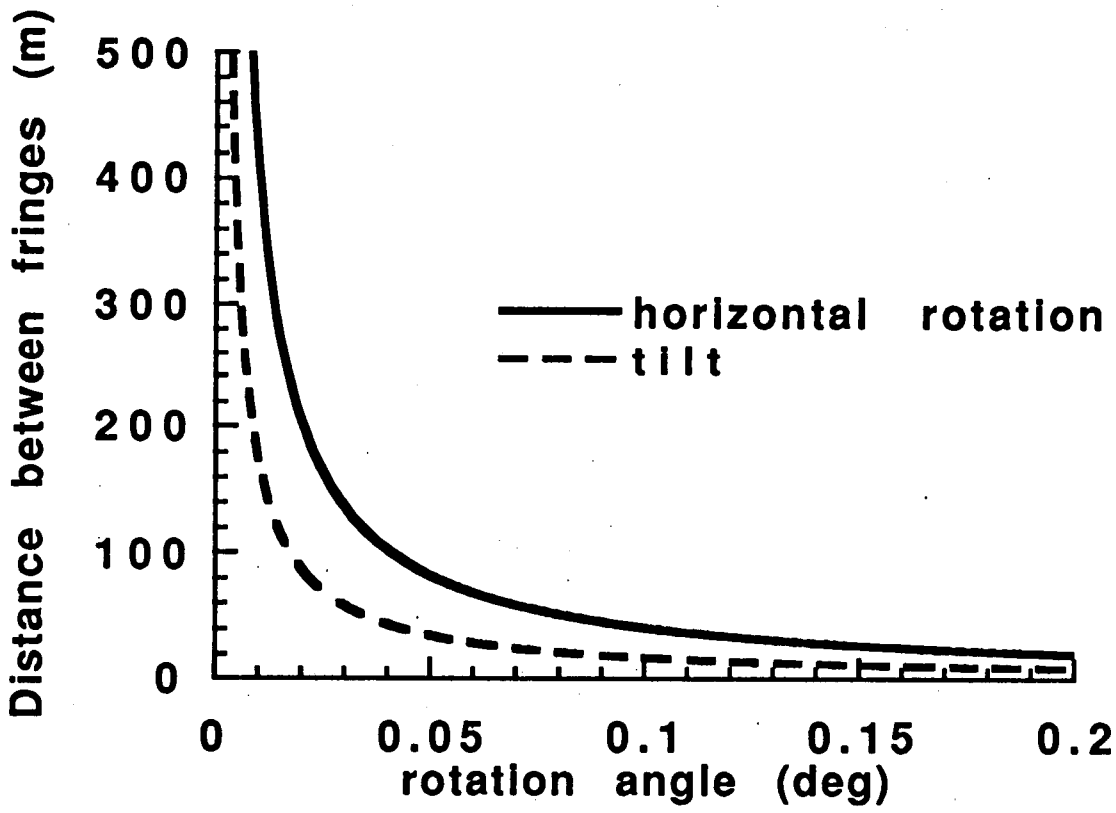
Distance between fringes (m)
500
400
300
200
100
0
horizontal rotation
tilt
0
0.05
0.1
0.15
0.2
rotation angle (deg)

Figure 3b

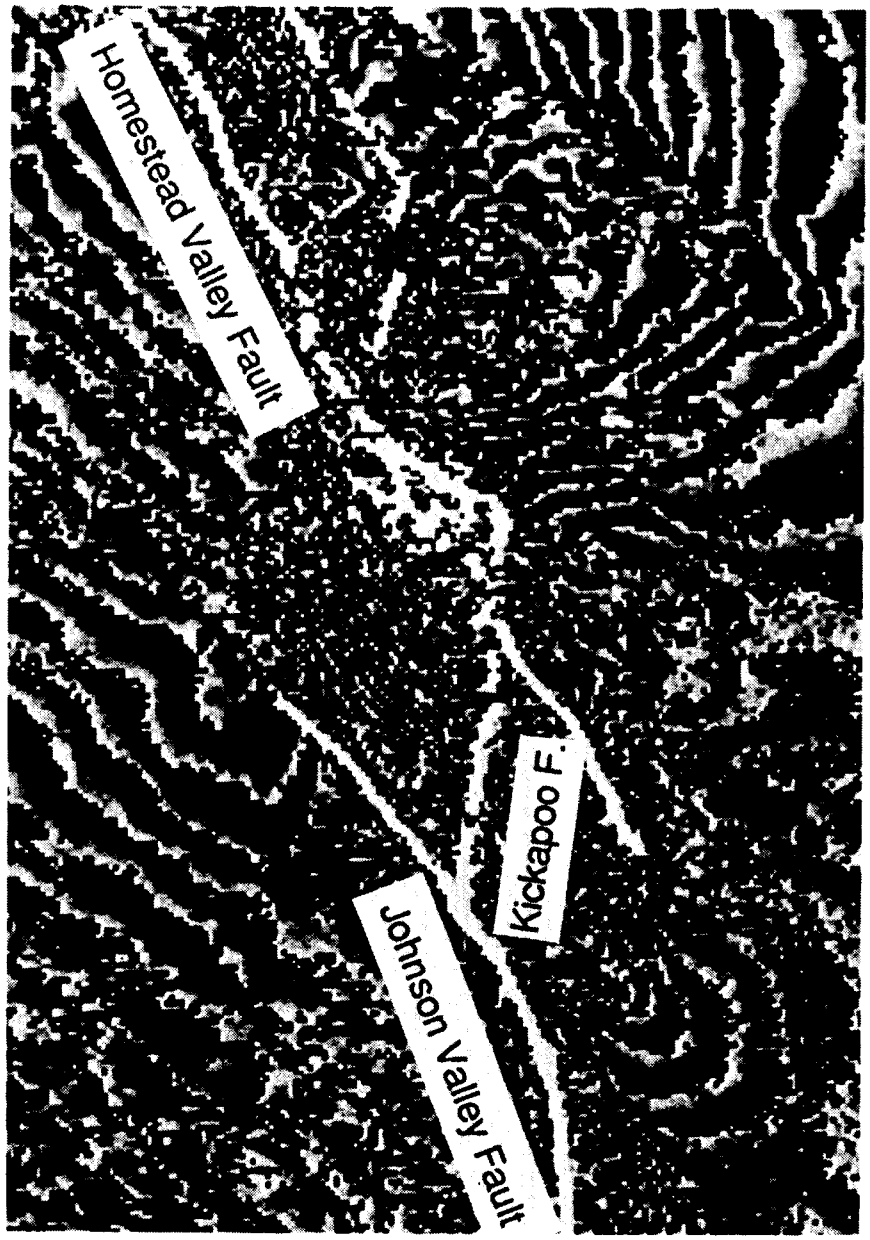

5 km

Figure 4

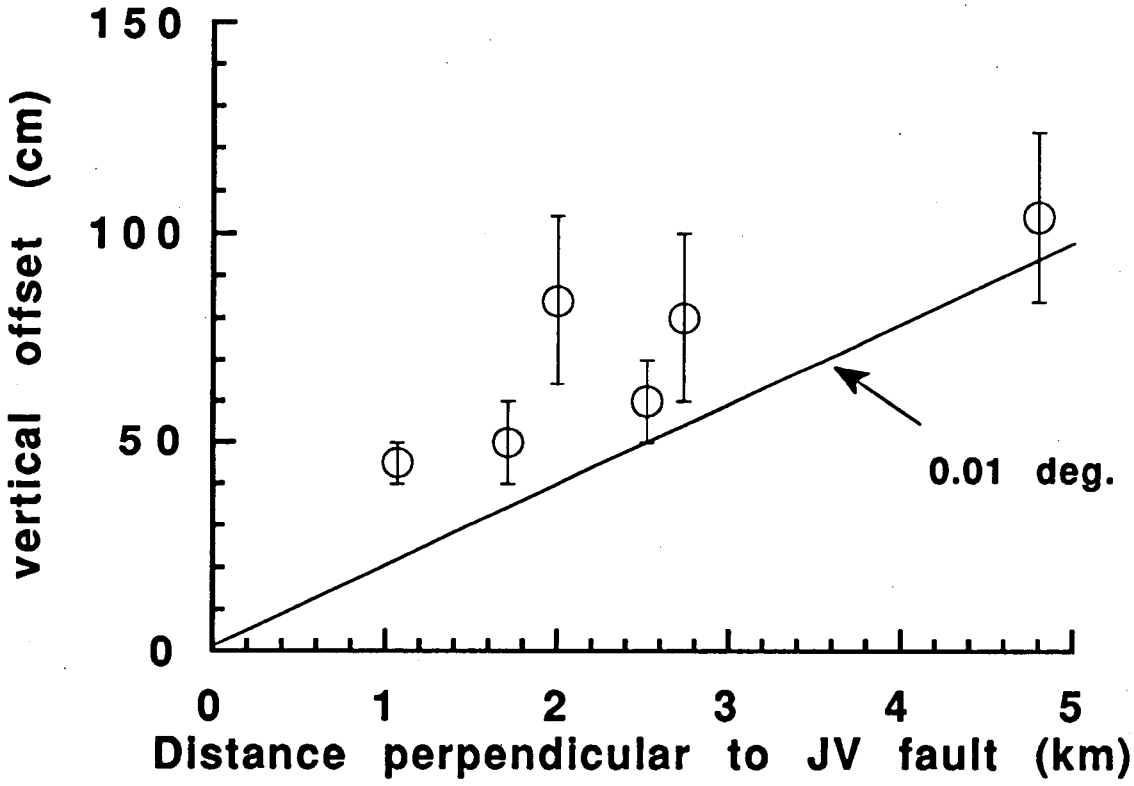
150
100
50
0
vertical offset (cm)
0.01 deg.
0
1
2
3
4
5
Distance perpendicular to JV fault (km)

Figure 5

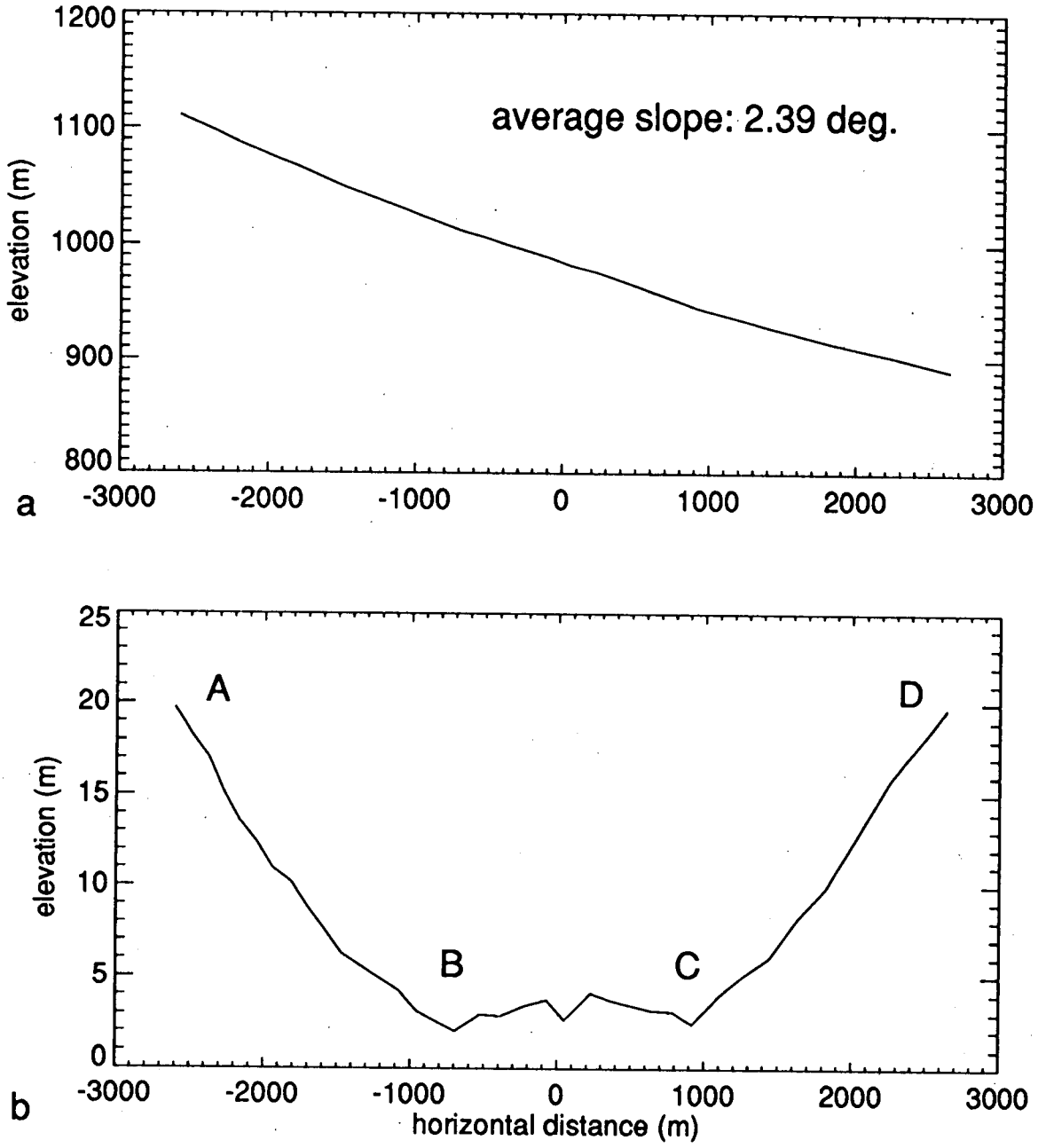
average slope: 2.39 deg.
elevation (m)
1200
1100
1000
900
800
a
-3000
-2000
-1000
0
1000
2000
3000
25
20
15
10
5
0
A
B
C
D
b
horizontal distance (m)

Figure 6

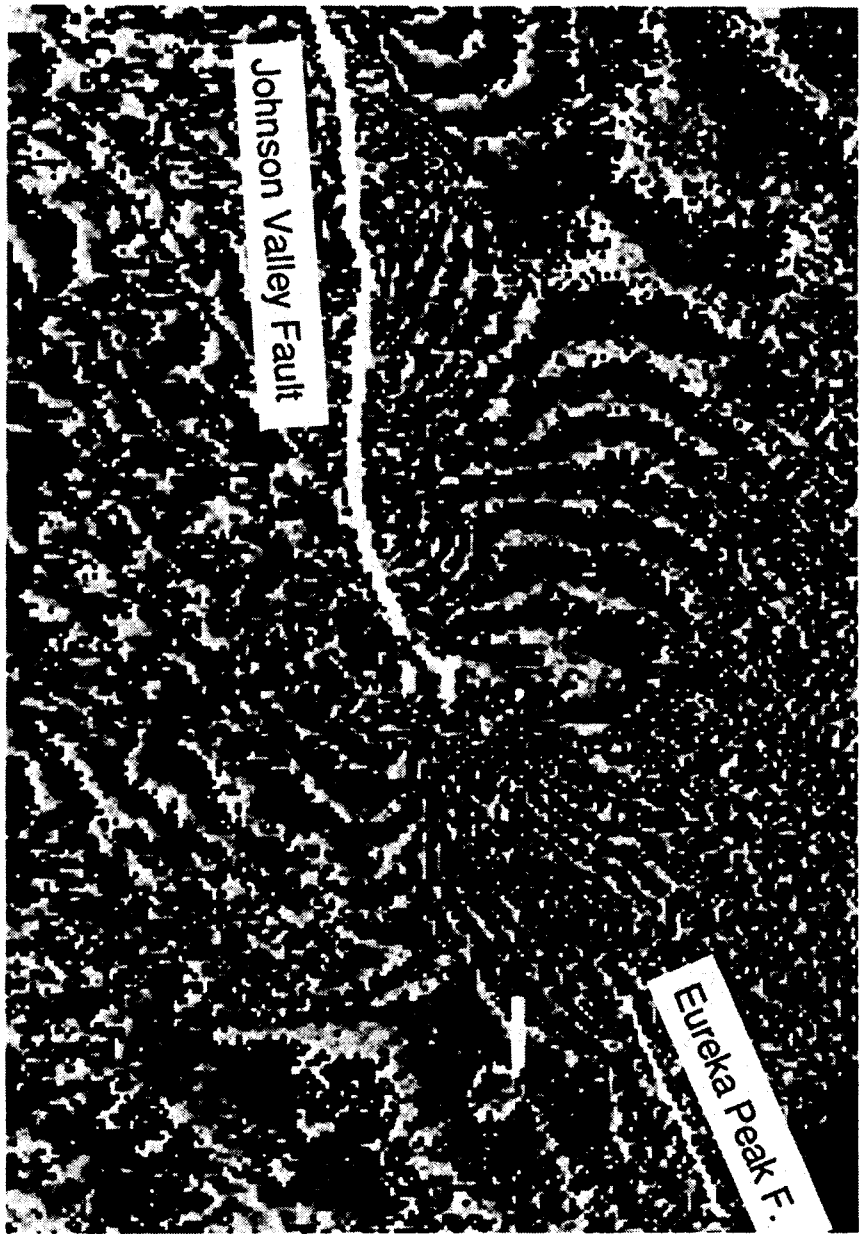

5 km

Figure 7

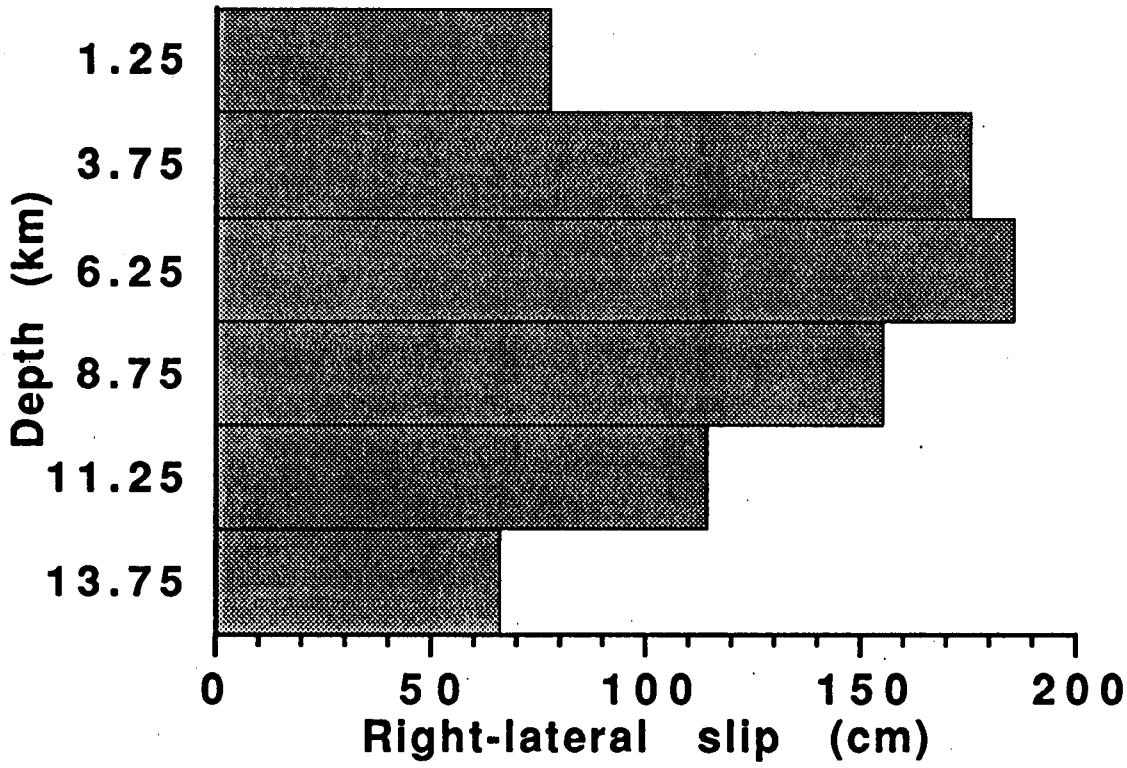
1.25
3.75
6.25
8.75
11.25
13.75
Depth (km)
0
50
100
150
200
Right-lateral slip (cm)

Figure 8